DAILY CYCLE OF THE SURFACE ENERGY BALANCE IN ANTARCTICA AND THE INFLUENCE OF CLOUDS

MICHIEL VAN DEN BROEKE*, CARLEEN REIJMER, DIRK VAN AS and WIM BOOT

Utrecht University, Institute for Marine and Atmospheric research (IMAU), PO Box 80005, 3508 TA Utrecht, The Netherlands

ABSTRACT

We present the summertime daily cycle of the Antarctic surface energy balance (SEB) and its sensitivity to cloud cover. We use data of automatic weather stations (AWS) located in four major Antarctic climate zones: the coastal ice shelf, the coastal and interior katabatic wind zone and the interior plateau. Absorbed short wave radiation drives the daily cycle of the SEB, in spite of the high surface albedo (0.84–0.88). The dominant heat sink is the cooling by long wave radiation, but this flux is distributed more evenly throughout the day so that a pronounced daily cycle in net all-wave radiation remains with all-sky night-time heat losses of 20–30 W m^{-2} and noontime heat gains of 30–40 W m^{-2}. During the night, heat is re-supplied to the snow surface by the sensible heat flux, especially in the katabatic wind zone, and the sub-surface heat flux. Daytime radiative energy excess is removed from the surface by sublimation (except at the high plateau) and sub-surface heat transport. Daytime convection occurs at all sites around solar noon but is generally weak. Spatial differences in the SEB are largely controlled by differences in cloud cover. Clouds are associated with higher surface temperatures and near-surface wind speeds. This especially limits nocturnal cooling, so that the strongest daytime convection is found during overcast conditions on the interior plateau. Copyright © 2006 Royal Meteorological Society.

KEY WORDS: Antarctica; meterology; surface energy balance

1. INTRODUCTION

The annual mean surface net radiation balance over the ice sheet of Antarctica is negative on average (Hatzianastassiou *et al*., 2004; Van den Broeke *et al*., 2004c), which leads to cooling of the near-surface air and a well-developed katabatic circulation. Under the influence of Coriolis forcing, Antarctic katabatic winds flow generally eastwards along the height contours of the ice sheet and are therefore sensitive to the strength of the mid-tropospheric westerlies (i.e. the polar vortex, Van den Broeke and van Lipzig, 2002), which some authors claim are themselves influenced by the katabatic circulation (Egger, 1985; Parish, 1992). A good knowledge of heat exchange at the Antarctic snow surface is therefore a prerequisite for a good understanding of regional and large-scale Antarctic climate and changes therein. Surface heat exchange is described by the surface energy balance (SEB), which for a snow surface can be written as:

$$M = SW{\downarrow} + SW{\uparrow} + LW{\downarrow} + LW{\uparrow} + SHF + LHF + G$$
$$= SW_{\text{net}} + LW_{\text{net}} + SHF + LHF + G$$
$$= R_{\text{net}} + SHF + LHF + G \qquad (1)$$

where M is melting energy ($M = 0$ if the surface temperature $T_s < 273.15$ K), $SW{\downarrow}$ and $SW{\uparrow}$ are the incoming and reflected short wave radiation fluxes, $LW{\downarrow}$ and $LW{\uparrow}$ are the incoming and emitted long wave

---

* Correspondence to: Michiel Van Den Broeke, Utrecht University, Institute for Marine and Atmospheric research (IMAU), PO Box 80005, 3508 TA Utrecht, The Netherlands; e-mail: broeke@phys.uu.nl

radiation fluxes, *SHF* and *LHF* are the turbulent fluxes of sensible and latent heat and *G* is the sub-surface heat flux. All terms are evaluated at the surface and are defined positive when directed towards the surface.

The summertime Antarctic SEB differs markedly from mid- and lower latitudes and also from the Arctic basin. The Antarctic atmosphere is highly transmissive for solar radiation, especially on the high interior plateau where the atmosphere is thin and the concentrations of clouds, water vapour and aerosol are low. Zhang *et al*. (2004) showed that $SW\downarrow$ in December has a strong peak over interior Antarctica, with daily mean values up to 450 W m^{-2}, while the corresponding June values over the Arctic basin are only about 300 W m^{-2}. However, over the dry and clean Antarctic snow surface, only 5–20% of the incident $SW\downarrow$ is absorbed; the high solar zenith angle and its small daily amplitude distribute the small absorbed energy relatively evenly over the day.

In spite of this, results from numerous dedicated off-pole meteorological experiments show a strong diurnal cycle of summertime Antarctic surface-layer climate and SEB (Liljequist, 1957; Ohata *et al*., 1985; Wendler *et al*., 1988; Heinemann and Rose, 1990; Van den Broeke and Bintanja, 1995; Bintanja and van den Broeke, 1995; Mastrantonio *et al*., 1999; Bintanja, 2000; Van As *et al*., 2005a; Argentini *et al*., 2005; King *et al*., 2006). Similar results have been reported on the basis of data from automatic weather stations (AWS, Kikuchi *et al*., 1988; Allison, 1985; Clow *et al*., 1988; Stearns and Weidner, 1993; Reijmer and Oerlemans, 2002; Renfrew and Anderson, 2002), as well as theoretical and numerical modelling studies (Gallée and Schayes, 1992; Parish *et al*., 1993; Sorbjan *et al*., 1986; Van As *et al*., 2006).

Global and regional atmospheric models still have difficulties in accurately representing the Antarctic SEB because of its extreme character and the lack of detailed observations. Typical problems occur in the radiation schemes in combination with simplified surface albedo parameterisations that have been developed for mid-latitude snow covers. Surface-layer stability functions are adjusted in such a way that turbulent exchange does not cease at high static stabilities, to avoid decoupling of the lower model layers from the free atmosphere, often leading to overestimated turbulent exchange (King and Connolley, 1997; King *et al*., 2001). Finally, parameterisation of surface roughness includes an orographic component, which leads to overestimated turbulent mixing in mountainous regions (Van Lipzig *et al*., 1999). To improve model performance over Antarctica, more observations of the Antarctic SEB are clearly needed.

Since December 1995, the Institute for Marine and Atmospheric Research of Utrecht University (UU/IMAU) together with partners from Germany, Sweden, the UK and Norway, has operated several AWS in western Dronning Maud Land, Antarctica. Data of these AWS have been used to assess the quality of unattended radiation measurements, to describe the Antarctic radiation climate (Van den Broeke *et al*., 2004b,c) and to quantify the various components of the surface mass and energy balance (Reijmer and Oerlemans, 2002; Van den Broeke *et al*., 2004a,d; Van den Broeke *et al*., 2005). In this paper, we use the data from four AWS to calculate the daily cycle of the summertime Antarctic SEB and study the influence of cloud cover. In Section 2 we present AWS locations, sensor specifications, data treatment methods and the SEB model. Section 3 presents results, followed by a discussion and summary in Section 4.

2. METHODS

2.1. *AWS description and sensor specifications*

The four AWS used in this study are situated along a traverse line in Dronning Maud Land, East Antarctica, connecting the coastal ice shelf (AWS 4) to the polar plateau (AWS 9) via the coastal (AWS 5) and inland (AWS 6) katabatic wind zone (Figure 1). In a radius of at least several kilometres, the surroundings of the AWS consist of undisturbed snow surfaces. Sensor specifications are given in Table I; location specifics and information on the average summer climate are given in Table II. AWS 4 is located on the flat Riiser-Larsen ice shelf some 80 km away from the ice shelf front and 40 km from the ice sheet grounding line. AWS 5 is located just inland of the grounding line, on the coastal slopes of the ice sheet. AWS 6 is situated further inland in a region with a similar surface slope. AWS 9 is situated on the interior plateau close to Kohnen base, where the surface is relatively flat. Average summertime surface temperature and specific humidity decrease with elevation (Table II), but relative humidity (RH) shows a minimum and wind speed a maximum

in the katabatic wind zone, owing to nocturnal slope flows and the associated adiabatic warming and drying of the air.

All four AWS are similar in design; a picture of AWS 9 is shown in Figure 2. Single-level measurements of wind, temperature and RH are performed at a height of 2.5–3 m on the date of installation. Air pressure is measured in the electronics enclosure, which is buried in the snow. A Kipp and Zonen CNR1 radiation sensor measures separately the four radiation components. Snow temperatures are measured at initial depths of 0.05, 0.1, 0.2, 0.4, 0.8, 2, 4, 6, 10 and 15 m. These depths, as well as the heights of the AWS instruments, change continuously as snow accumulates or ablates from the surface; these height/depth changes are monitored with
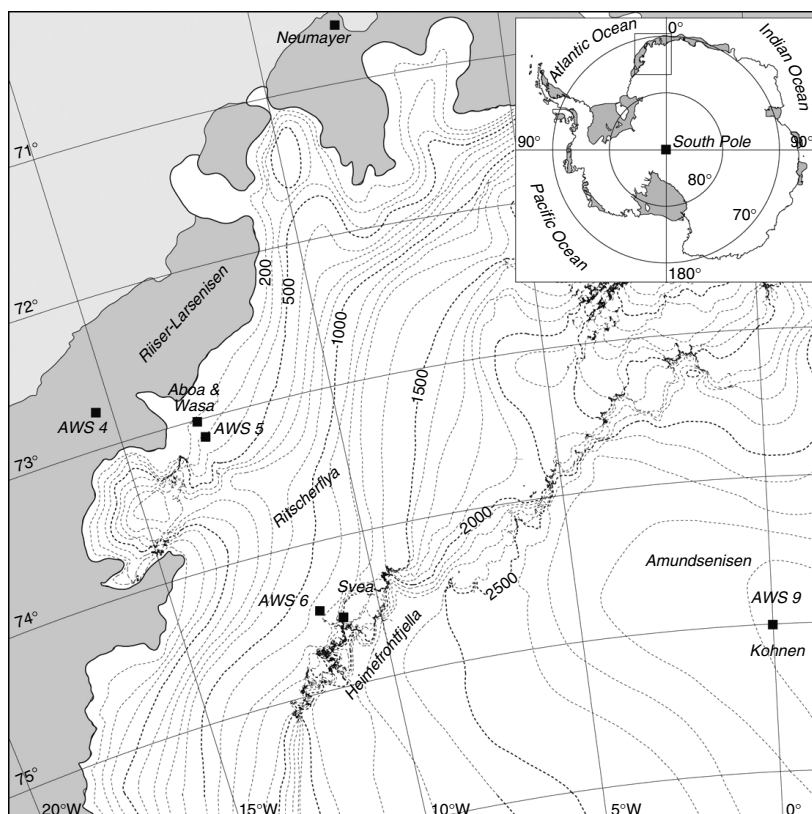

Figure 1. Map of western Dronning Maud Land, Antarctica, with AWS locations, main topographical features, ice shelves (grey), height contours (dashed lines, every 100 m) and station locations

Table I. AWS sensor specifications. EADT = estimated accuracy for daily totals

Sensor	Type	Range	Accuracy
Air pressure	Vaisala PTB101B	600 to 1060 hPa	4 hPa
Air temperature	Vaisala HMP35AC	−80 to +56 °C	0.3 °C
Relative humidity	Vaisala HMP35AC	0 to 100%	2% (RH < 90%)
			3% (RH > 90%)
Wind speed	Young 05103	0 to 60 m s^{-1}	0.3 m s^{-1}
Wind direction	Young 05103	0 to 360°	3°
Pyranometer	Kipp en Zonen CM3	305 to 2800 nm	EADT +/− 10%
Pyrradiometer	Kipp en Zonen CG3	5000 to 50 000 nm	EADT +/− 10%
Snow height	Campbell SR50	0.5 to 10 m	0.01 m or 0.4%

Table II. AWS topographic and climate characteristics for summer (Julian days 296 to 51), 1998–2001. If no measurement height is specified, the mean value at the AWS sensor level is used

|	AWS 4	AWS 5	AWS 6	AWS 9
Location				
Latitude	72° 45.2′S	73° 06.3′S	74° 28.9′S	75° 00.2′S
Longitude	15° 29.9W	13° 09.9W	11° 31.0W	0°00.4E
Elevation (m asl)	34	363	1160	2892
Surface slope (m km^{-1})	<1	13.5	15	1.3
Period of operation used for this paper				
Start of observation	22 Dec 1997	3 Feb 1998	14 Jan 1998	1 Jan 1998
End of observation	21 Dec 2001	2 Feb 2002	13 Jan 2002	31 Dec 2001
Basic climate variables (averaged for Julian days 296 to 51)				
Surface temperature (K)	264.7	263.7	259.3	242.4
Relative humidity (%)	89	82	75	91
Specific humidity (g kg^{-1})	1.91	1.71	1.22	0.39
10 m wind speed (m s^{-1})	6.1	7.0	6.6	5.0
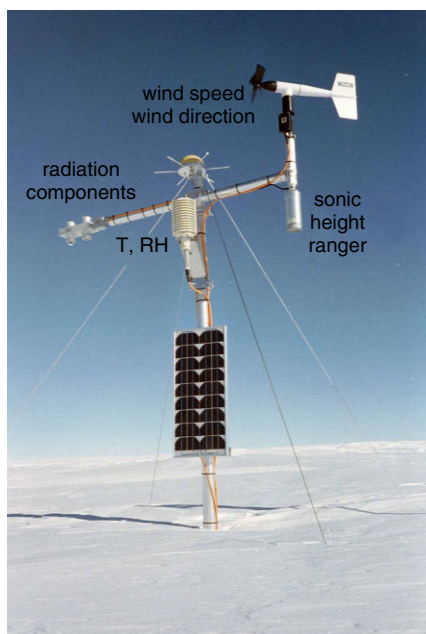
Figure 2. Picture of AWS 9, taken four years after installation, after approx. 1 m of snow accumulation. The data logger and pressure sensor are in the electronics enclosure, buried in the snow. The other AWS have similar designs. This figure is available in colour online at www.interscience.wiley.com/ijoc

a sonic height ranger. The sampling interval for pressure is 30 min (instantaneous value); all other sensors are sampled at 6-min intervals (instantaneous, except for wind speed, which is cumulative) after which 2-h averages are calculated and stored in a Campbell CR10 data logger with separate memory modules.

2.2. AWS data treatment

Data from Antarctic AWS suffer from potentially large errors. However, detailed, on-site comparison experiments (Bintanja, 2000; Van As *et al*., 2005b) have shown that most problems have now been adequately

addressed with improved measurement techniques and data treatment methods. For an accurate daily cycle of SEB components, a necessary correction is the 'accumulated albedo' method (Van den Broeke *et al.*, 2004c) and the correction for RH at temperatures below the factory specifications (Anderson, 1994).

2.3. Energy balance model: description

Equation (1) describes the SEB of a 'skin' layer without heat capacity, the temperature of which reacts instantaneously to a change in energy input. By assuming Equation (1) to be valid, we neglect the effects of precipitation adding/removing heat from the surface and penetration of short wave radiation into the snow pack. The latter assumption is justified for the fine-grained, dry Antarctic snow (Brandt and Warren, 1993). The SEB model has an atmospheric and sub-surface module. Two SEB components (SW_{net} and $LW\downarrow$) are taken directly from (corrected) observations. In the atmospheric part of the model, *SHF* and *LHF* follow from:

$$SHF = -\rho c_{p}\overline{(w'\theta')}_{s} = \rho c_{p}u_{*}\theta_{*}$$
$$LHF = -\rho L_{s}\overline{(w'q')}_{s} = \rho L_{s}u_{*}q_{*} \tag{2}$$

where ρ is the air density, c_{p} the heat capacity of dry air at constant pressure, L_{s} the latent heat of sublimation, w', θ' and q' are the turbulent fluctuations of vertical velocity, potential temperature and specific humidity and u_{*}, θ_{*} and q_{*} are the associated turbulent scales. The turbulent scales are calculated using the 'bulk' method, a robust method that relates turbulence scales to differences in wind speed V, potential temperature θ and specific humidity q between a single measurement level and the snow surface:

$$u_{*} \cong \frac{\kappa[V(z_{V}) - V(z_{0,V})]}{\ln\frac{z_{V}}{z_{0,V}} - \Psi_{m}\left(\frac{z_{V}}{L}\right)}$$

$$\theta_{*} \cong \frac{\kappa[\theta(z_{T}) - \theta(z_{0,T})]}{\ln\frac{z_{T}}{z_{0,T}} - \Psi_{h}\left(\frac{z_{T}}{L}\right)}$$

$$q_{*} \cong \frac{\kappa[q(z_{q}) - q(z_{0,q})]}{\ln\frac{z_{q}}{z_{0,T}} - \Psi_{h}\left(\frac{z_{q}}{L}\right)} \tag{3}$$

where L is the Obukhov length scale:

$$L = \frac{u_{*}^{2}}{\kappa g/\theta\,[\theta_{*} + 0.62\theta q_{*}]} \tag{4}$$

and κ is the Von Kármán constant ($\kappa = 0.4$) and V, θ and q are the wind speed, potential temperature and specific humidity measured at AWS sensor heights z_{V}, z_{T} and z_{q}, respectively. The RH- and T sensors are in the same housing, so that $z_{q} = z_{T}$, while z_{V} is greater by about 0.75 m (Figure 2). Sensor heights (z_{V}, z_{q} and z_{T}) continuously change owing to accumulation/ablation at the snow surface and are continuously tracked using data from the sonic height ranger. Ψ_{m} and Ψ_{h} are the vertically integrated stability correction functions for momentum and heat, respectively. For stable conditions ($z/L > 0$) we use $\Psi_{m} = \Psi_{h}$ and the functional form proposed by Holtslag and De Bruijn (1988), which behaves most consistently in the very stable limit where turbulence ceases (Andreas, 2002). For unstable conditions ($z/L < 0$) the functions of Dyer (1974) are used. The surface roughness length for momentum ($z_{0,V}$) was derived from on-site eddy-correlation measurements near AWS 6 ($z_{0,V} = 0.16$ mm) and near AWS 9 ($z_{0,V} = 0.021$ mm) (Van den Broeke *et al.*, 2005). For AWS 5, which has a climate similar to AWS 6, we used $z_{0,V} = 0.16$ mm; for AWS 4 we used $z_{0,V} = 0.1$ mm in line with the values reported from the nearby ice shelf stations Halley and Neumayer (King and Anderson, 1994; Heinemann, 1988). The temporal variation of $z_{0,V}$ is at present

unknown and we assume it to be constant in time. For the calculation of the scalar roughness lengths for heat and moisture, we applied the expressions derived from the surface renewal model by Andreas (1987).

In the sub-surface module, heat conduction in the snow is calculated by solving the one-dimensional heat-transfer equation on grid levels spaced 0.04 m apart down to a depth of 20 m, below which heat conduction is assumed to vanish. The thermal conductivity of snow is assumed to be a function of snow density, according to Anderson (1976). Snow density was measured during maintenance visits to the AWS. The conductive heat flux at the surface, G, is extrapolated upwards from its sub-surface values at 2 and 6 cm depth. At the start of the model run, the snow temperature profile is initialised using AWS snow temperature data. Equation (1) can now be solved, using bisection and several iterative loops, for surface temperature T_s. The full solving procedure is summarised in Van den Broeke *et al.* (2004d).

2.4. Energy balance model: performance

The combined performance of the data treatment methods and the SEB model can be checked by comparing observed and modelled average diurnal cycles of *SHF* and *LHF* (Figure 3). Eddy-correlation measurements of *SHF* and *LHF* were performed during two summer experiments at Svea near AWS 6 (duration 23 days, Bintanja, 2000) and at Kohnen near AWS 9 (period length 28 days, Van As *et al.*, 2005b). These data were reduced to 2-hourly means to match the AWS time resolution. At AWS 9, the 'observed' *LHF* was calculated using the modified Bowen ratio method. Figure 3 shows a close agreement between the observed and modelled fluxes; correlations coefficients range between 0.93 and 0.97 with slopes equal to unity within the margins of uncertainty. Note that the large day-to-day differences, which are mainly caused by differences in cloud cover and large-scale circulation, are also well captured, although the modelled daytime convection is overestimated towards the end of both periods. Alternatively, Van den Broeke *et al.* (2004d) showed that the modelled and observed T_s (the latter derived from $LW\uparrow$, assuming the snow surface to have unit emissivity) differed generally by less than 1 K. We may conclude that the model is capable of reliably simulating the amplitude and phase of the diurnal cycle of the summertime Antarctic SEB.

2.5. Average diurnal cycle: selection criteria

The average summertime daily cycle was calculated for the four-year period 1997/1998 to 2000/2001. The averaging period was defined as the 120-day period surrounding the summer solstice (23rd of October to the 20th of February); this includes all days in which the sun does not set for longer than 4 h (two data points in the AWS climate series). This data set is of a length sufficient for large sub-samples to be selected, for instance, to study the influence of cloudiness, without introducing significant bias with respect to top-of-atmosphere (TOA) radiation (i.e. the sub-samples are approximately normally distributed with respect to TOA radiation). In the remainder of the paper, the average diurnal cycle will be plotted as a function of time, where 12 h equals solar noon, not local time.

Apart from average conditions, we distinguish 'clear-sky' and 'overcast' conditions. Cloud cover is estimated on the basis of net long wave radiation (LW_{net}) and temperature. Polynomial fits through the 5th and 95th percentile levels of LW_{net}, plotted as a function of temperature, are assumed to represent clear-sky and overcast conditions, respectively, with a linear interpolation for cloudiness values in between. In practice, $LW_{net} = 0$ represents overcast conditions for all temperatures, while for clear-sky conditions LW_{net} decreases with increasing temperatures (Van den Broeke *et al.*, 2004c). The cloud cover thus obtained can be compared to on-site observations near AWS 6 and AWS 9 (Figure 4). The parameterised cloud cover follows the observations, but has smaller temporal variability. This is perhaps not surprising, as the observed cloud cover is insensitive to cloud optical thickness, while parameterised cloud cover is mainly sensitive to the optical thickness. In the remainder of this paper, cloud cover and therefore N refers to optical thickness rather than fractional sky cover.

Using this method, the frequency distributions of N were calculated (Figure 5). In the following, 'clear-sky' is defined as the average of all days where daily mean estimated $N < 0.3$ and the 'overcast' daily cycle is defined as the average of all days where daily mean estimated $N > 0.7$. Note that, for example, the sample
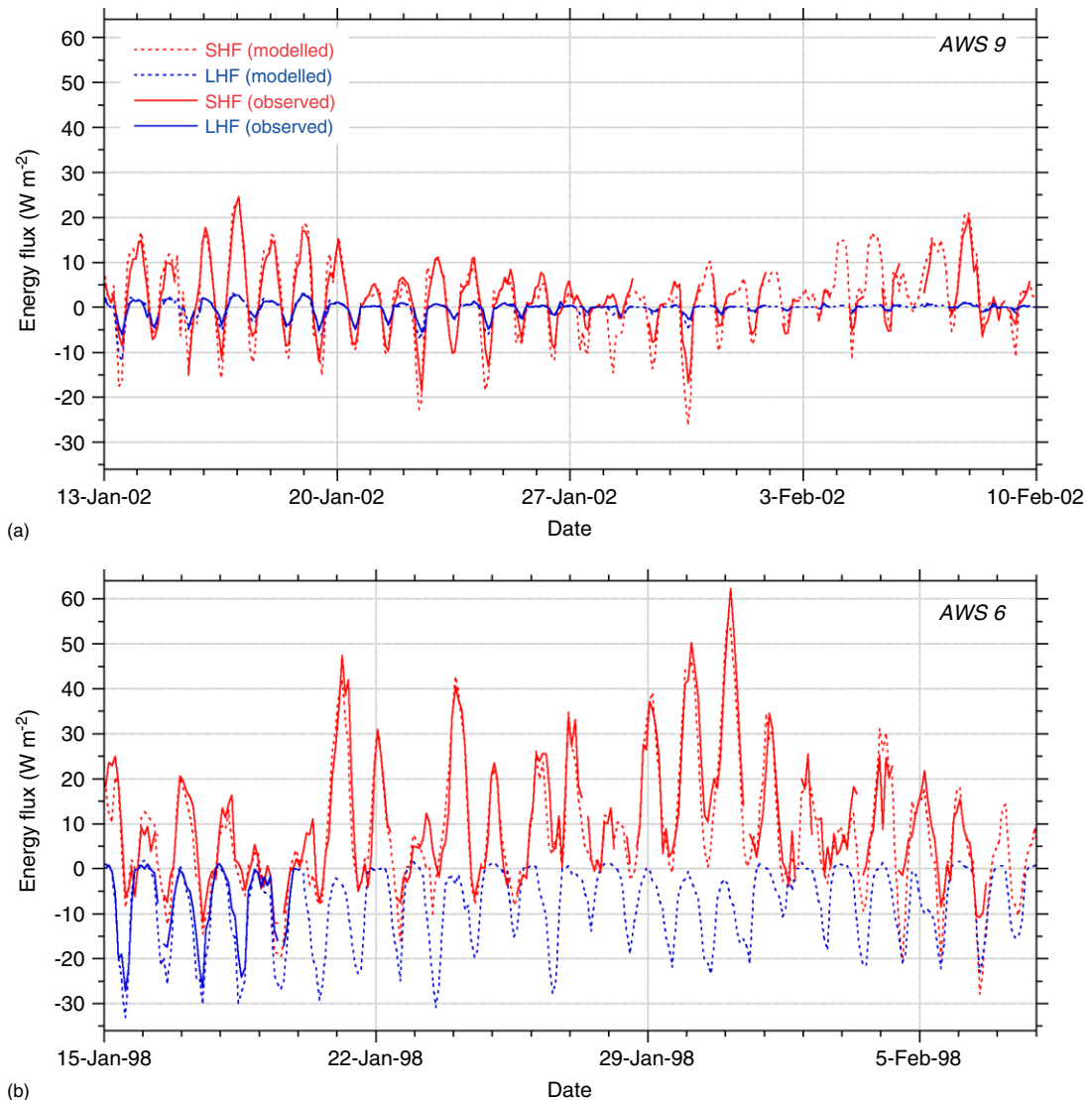
Figure 3. Modelled *versus* observed *SHF* and *LHF* for summer experiments at (a) Kohnen base near AWS 9 in 2002 and (b) Svea station near AWS 6 in 1998. This figure is available in colour online at www.interscience.wiley.com/ijoc

of overcast conditions at AWS 4 represents four times as much data as that at AWS 9 (36% *vs* 9%) and that clear-sky conditions occur twice as frequently at AWS 9 (57%) as at AWS 4 (24%).

3. RESULTS

Results for all-sky, clear-sky and overcast conditions are summarised in the following tables and figures: Table II lists averages of the basic climate variables: surface temperature, 2 m specific and relative humidities and 2 m wind speed. Table III lists average values of cloud cover N, surface albedo α, atmospheric transmissivity for short wave radiation τ and net absorbed fraction at the surface $\tau (1 - \alpha)$. Table IV lists daily average SEB values. Average daily cycles of temperature, specific humidity and wind speed are presented in Figure 6; average daily cycles of SW_{net} and LW_{net} in Figure 7 and average daily cycles of the turbulent scales
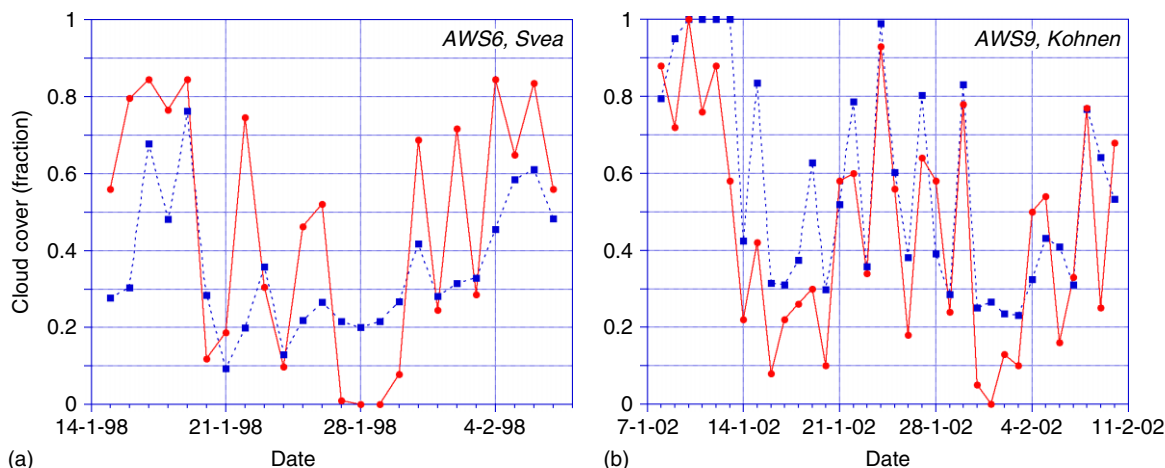
Figure 4. Observed (solid lines) and parameterised (dashed lines) cloud cover for (a) AWS 6 and (b) AWS 9. This figure is available in colour online at www.interscience.wiley.com/ijoc

Table III. Average cloud cover, N, atmospheric transmissivity for short wave radiation, τ, surface albedo, α, and net absorbed fraction at the surface, $\tau(1-\alpha)$, for all-sky, clear-sky and overcast conditions. Averages are calculated for Julian days 296 to 51, 1998–2001. For readability, all numbers have been expressed as percentages, i.e. multiplied by 100

	AWS 4	AWS 5	AWS 6	AWS 9
All-sky				
N	54	47	46	33
τ	64.3	67.9	73.2	78.5
α	87.7	84.3	84.2	84.5
$\tau(1-\alpha)$	7.9	10.7	11.6	12.2
Clear-sky				
N	16	17	21	18
τ	75.8	78.8	83.0	82.7
α	84.9	81.3	81.7	83.6
$\tau(1-\alpha)$	11.4	14.7	15.2	13.6
Overcast				
N	85	84	83	79
τ	54.1	54.0	56.4	62.5
α	90.7	89.2	89.0	87.1
$\tau(1-\alpha)$	5.0	5.8	6.2	8.1

for momentum, heat and moisture in Figure 8 for all-sky (solid lines), clear-sky (dotted lines) and overcast (dash-dotted lines) conditions. The average daily cycles of SEB components are presented in Figure 9.

3.1. Wind speed, temperature and humidity

The katabatic wind climate at AWS 5 and 6 is evident from relatively high wind speed and low RH (Table II), caused by downward advection and subsequent heating/drying of the air. The largest all-sky wind speeds are found at AWS 5 and 6, where the night-time maximum is a clear katabatic signature. AWS 6 shows a double wind speed maximum, compared to a single daytime wind speed maximum at AWS 4 and 9
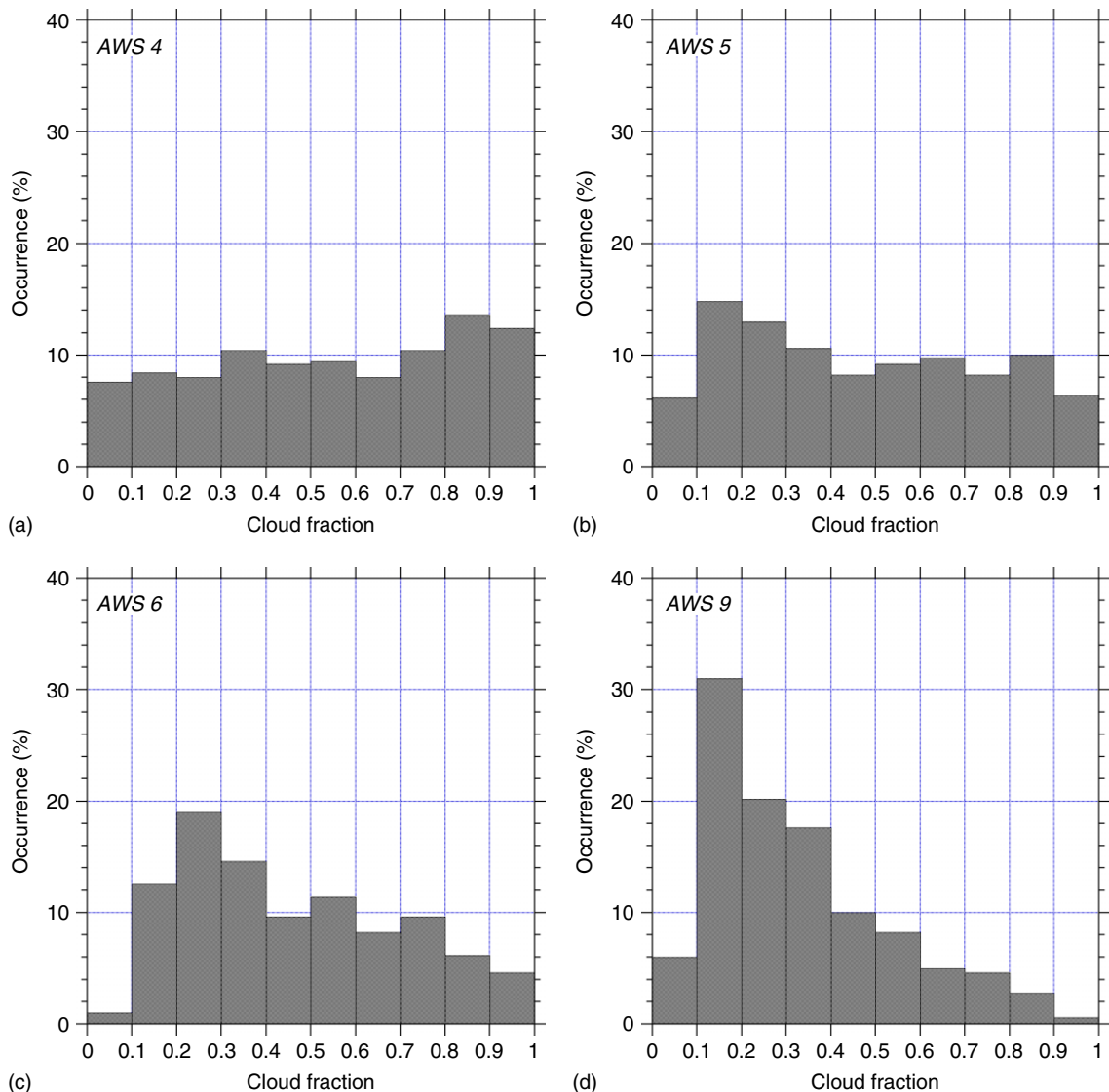
Figure 5. Frequency distribution of cloud cover (in tenths) estimated from net long wave radiation for (a) AWS 4, (b) AWS 5, (c) AWS 6 and (d) AWS 9. This figure is available in colour online at www.interscience.wiley.com/ijoc

(Figure 6). AWS 9 has the largest all-sky amplitude of the daily surface temperature cycle (10 K, Figure 6). Because of the low temperatures, absolute values and daily cycle of specific humidity are small; it mainly follows the temperature, as the daily cycle in RH (not shown) is <10% and has a minimum in the afternoon.

During clear-sky conditions, the daily cycle of surface temperature increases at all sites, with the biggest change at AWS 4 (Figure 6). As a result of the 'radiation paradox' (see Section 4), clear-sky temperatures are lower than all-sky values, except for a short period around noon at AWS 5. Clear-sky wind speeds are also lower and have a larger daily cycle; this reflects the reduced strength of the large-scale wind and the increased importance of nocturnal katabatic forcing at AWS 5 and 6 and night-time stability-related curvature of the wind speed profile at AWS 4 and 9.

Overcast conditions are associated with depression activity, and cause an increase in temperature, specific humidity and wind speed, with the largest changes at AWS 9, where clouds are rare (Figure 5). The strongest winds again occur at AWS 5 and 6, but the double wind speed maximum at the latter site no longer exists.
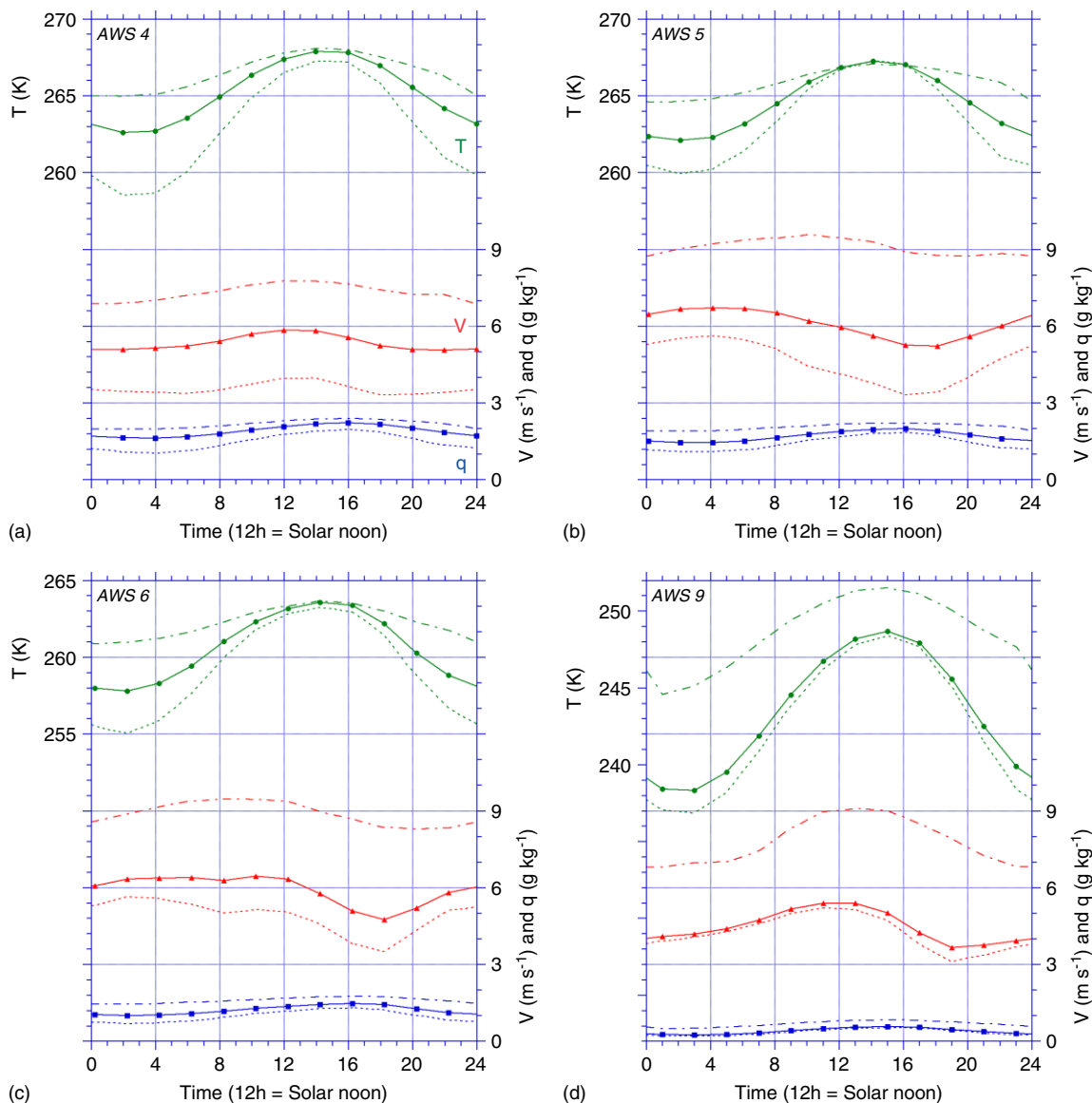
Figure 6. Average daily cycle of surface temperature (T), 2 m wind speed (V) and specific humidity (q) for all-sky (solid lines), clear-sky (dotted lines) and overcast conditions (dash-dotted lines) at (a) AWS 4, (b) AWS 5, (c) AWS 6 and (d) AWS 9. This figure is available in colour online at www.interscience.wiley.com/ijoc

Overcast conditions strongly reduce the daily temperature cycle, mainly by increasing night-time temperatures; only at AWS 9 does a significant increase in daytime temperature occur. Note that AWS 9 retains a considerable daily temperature cycle under overcast conditions (7 K) compared to the other sites (2–3 K). This is also valid for wind speed, and results from the smaller optical depth of the clouds over interior Antarctica and the lesser impact these have on the surface radiation balance (see next section).

3.2. Net shortwave radiation (SW_{net})

In spite of the high albedo, SW_{net} is the most important surface heat gain in the summertime SEB (Table IV). For all-sky conditions, SW_{net} decreases from 56 W m^{-2} at AWS 9 to 36 W m^{-2} at AWS 4, mainly because N
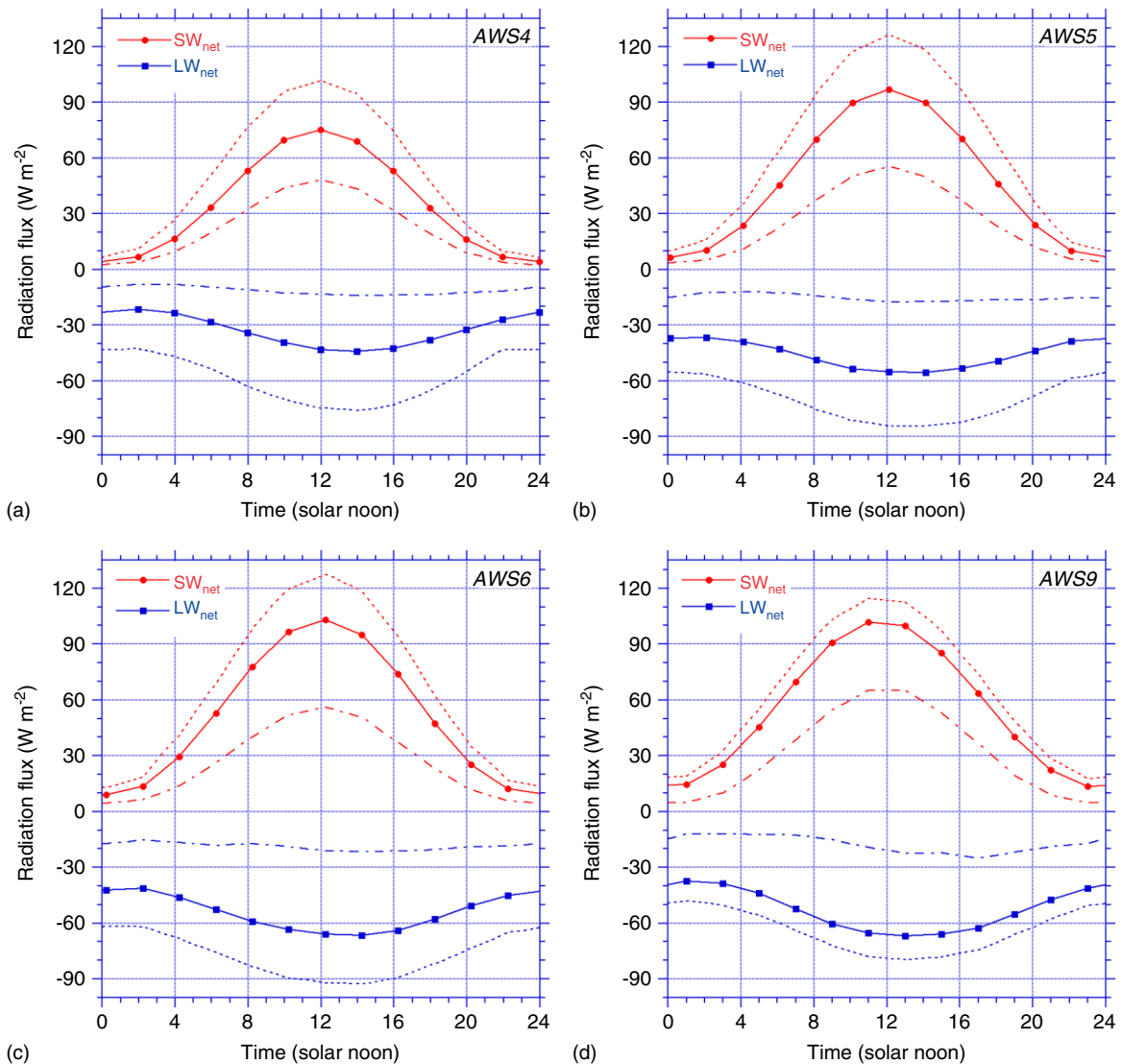
Figure 7. Average daily cycle of net shortwave radiation (SW_{net}, upper traces) and net longwave radiation (LW_{net}, lower traces) for all-sky (solid lines), clear-sky (dotted lines) and overcast conditions (dash-dotted lines) at (a) AWS 4, (b) AWS 5, (c) AWS 6 and (d) AWS 9. This figure is available in colour online at www.interscience.wiley.com/ijoc

increases from the interior towards the coast (from 33 to 54%) and τ decreases (from 79 to 64%, Table III), while α is highest at AWS 4 (see Section 4). The result is that the all-sky net absorbed fraction (Table III) is 1/3 smaller at AWS 4 (7.9%) than at AWS 9 (12.2%). The daily cycle of SW_{net} (Figure 7) shows noontime maxima from 75 W m^{-2} at AWS 4 to >100 W m^{-2} at the other stations, and midnight minima from 5 W m^{-2} at AWS 4 to 15 W m^{-2} at AWS 9, caused by differences in cloud cover and latitude.

Under clear-sky conditions, the net absorbed fraction (Table III) as well as average SW_{net} (Table IV) is largest in the katabatic wind zone, where clear-sky α is lowest. Under overcast conditions, a drop in τ and an increase in α are found at all sites (Table III), in such a way that α monotonously increases and τ decreases from the interior towards the coast. At AWS 4, where $\alpha > 0.9$, overcast conditions result in an absolute minimum in the net absorbed fraction (5.0%). In relative sense, the strongest reduction in overcast net absorbed fraction compared to clear-sky and all-sky conditions is found in the katabatic wind zone, owing to the sharp increase in albedo.
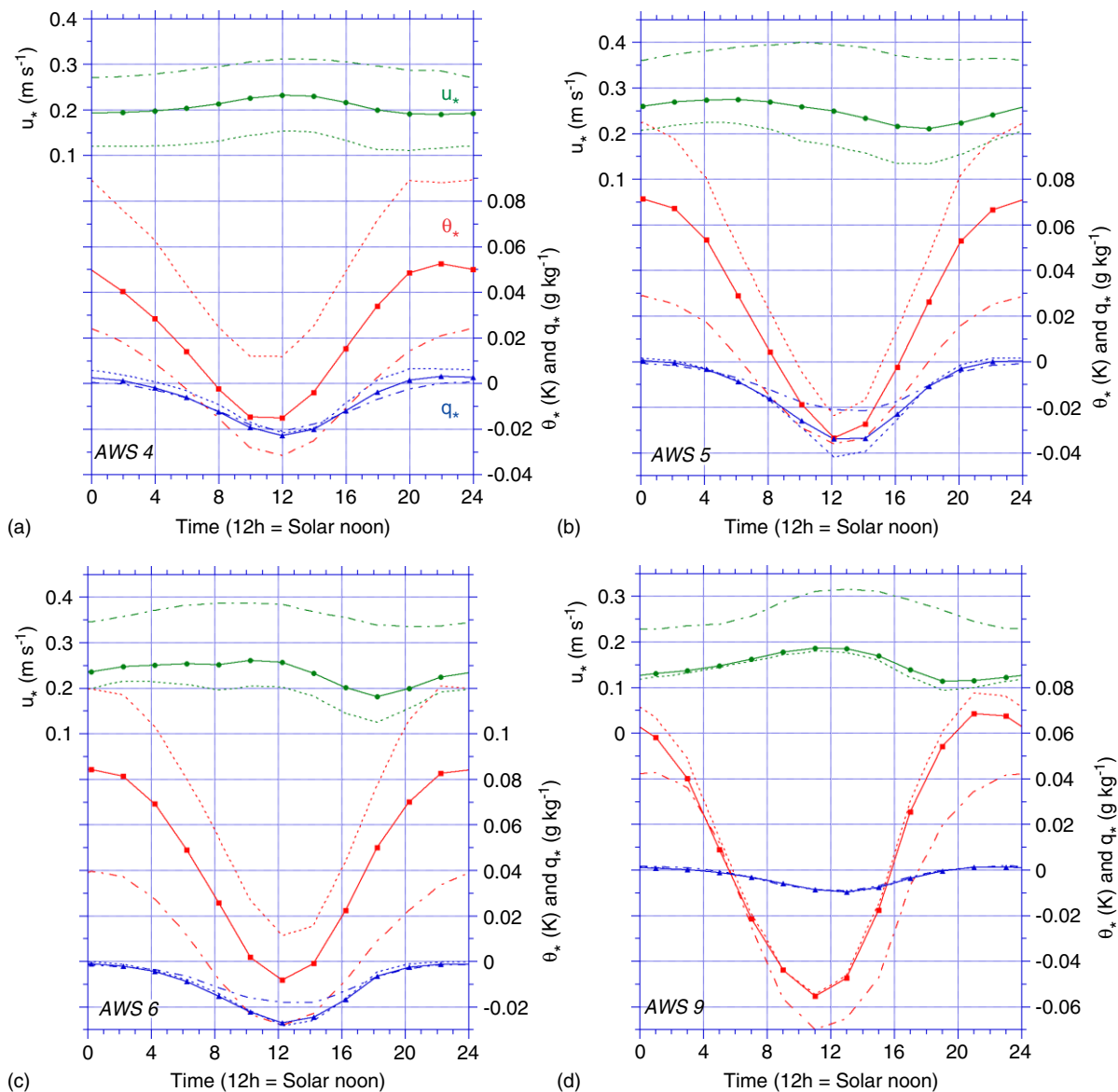
Figure 8. Average daily cycle of turbulent velocity scale (u_*, upper traces), turbulent temperature scale (θ_*, middle traces) and turbulent moisture scale (q_*, lower traces) for all-sky (solid lines), clear-sky (dotted lines) and overcast conditions (dash-dotted lines) at (a) AWS 4, (b) AWS 5, (c) AWS 6 and (d) AWS 9. This figure is available in colour online at www.interscience.wiley.com/ijoc

3.3. Net longwave radiation (LW_{net})

LW_{net} is the most important surface heat sink (Table IV) and attains its lowest all-sky values at the higher altitude sites of AWS 6 and 9, where cloud cover is lowest. The daily cycle of all-sky LW_{net} attains an afternoon minimum of -45 W m^{-2} (AWS 4) to -70 W m^{-2} (AWS 9), when surface temperature is at a maximum (Figure 7). Night-time values range from -20 W m^{-2} (AWS 4) to -40 W m^{-2} in the katabatic wind zone. Clear-sky LW_{net} shows a sharp drop compared to all-sky conditions, with afternoon values reaching -75 W m^{-2} at AWS 4 to -90 W m^{-2} at AWS 6. Night-time values range between -40 W m^{-2} at AWS 4 and -60 W m^{-2} at AWS 6. Under overcast conditions, daily average LW_{net} increases to values of -10 to -20 W m^{-2} (Table IV), and the daily cycle is damped (Figure 7); only at AWS 9 does the daily cycle still

Table IV. Average SEB components for all-sky, clear-sky and overcast conditions. Averages are calculated for Julian days 296 to 51, 1998–2001. All values are in W m^{-2}

	AWS 4	AWS 5	AWS 6	AWS 9
All-sky				
SW_{net}	36	49	53	56
LW_{net}	−33	−46	−55	−53
R_{net}	3	3	−2	3
SHF	4	7	11	1
LHF	−5	−8	−7	−1
G	−2	−2	−2	−3
Clear-sky				
SW_{net}	52	66	68	65
LW_{net}	−59	−71	−78	−64
R_{net}	−7	−5	−10	1
SHF	8	12	16	1
LHF	−2	−7	−6	−1
G	1	0	0	−1
Overcast				
SW_{net}	22	26	27	32
LW_{net}	−11	−15	−19	−18
R_{net}	11	11	8	14
SHF	0	1	4	−2
LHF	−6	−7	−7	−2
G	−5	−5	−5	−10

exceed 10 W m^{-2}. Compared to all-sky conditions, the increase in LW_{net} in the afternoon is 30 W m^{-2} (AWS 4) to more than 45 W m^{-2} (AWS 6 and 9). During the night the change is more modest, 10 W m^{-2} (AWS 4) to 25 W m^{-2} (AWS 6 and 9).

3.4. Sensible heat flux (SHF)

Figure 8 shows the daily cycle of θ_* and u_*, the turbulent scales that determine SHF. The daily cycle of u_* in first order reflects variations in wind speed (Figure 6), and is modified only in second order by spatial differences in $z_{0,V}$ and static stability effects. For example, owing to static stability effects, the night-time maximum in u_* in the katabatic wind zone is less pronounced than in the wind speed. The largest u_* values are found in the katabatic wind zone (AWS 5 and 6), where wind speeds are relatively high and the surface is roughest. As with wind speed, u_* decreases under clear-sky conditions and increases under overcast conditions at all sites.

More interesting is the behaviour of θ_* (Figure 8). For all-sky conditions, all sites show a period centred at the solar noon with statically unstable conditions ($\theta_* < 0$). The duration of this period differs markedly among the sites; it is shortest at AWS 6 (4 h) and longest at AWS 9 (10.5 h). The first-order influence of clouds is to displace the θ_* curve vertically rather than to adjust its amplitude. Under clear-sky conditions, the period with unstable stratification disappears at AWS 4 and 6 and becomes much shorter and less significant at AWS 5. Clear-sky night-time stability significantly increases at all sites (larger θ_*). Conversely, cloudy conditions enhance the duration and intensity of the daytime convective period and decrease night-time stability at all sites.

The all-sky daily cycle of SHF (Figure 9) mimics θ_*: SHF becomes most negative at AWS 9 (−10 W m^{-2}) where, as a result, a shallow but well-defined mixed layer of roughly 100 m depth can develop (Van As *et al.*, 2006). At night, wind shear must overcome the static stability in the surface layer, and the magnitude
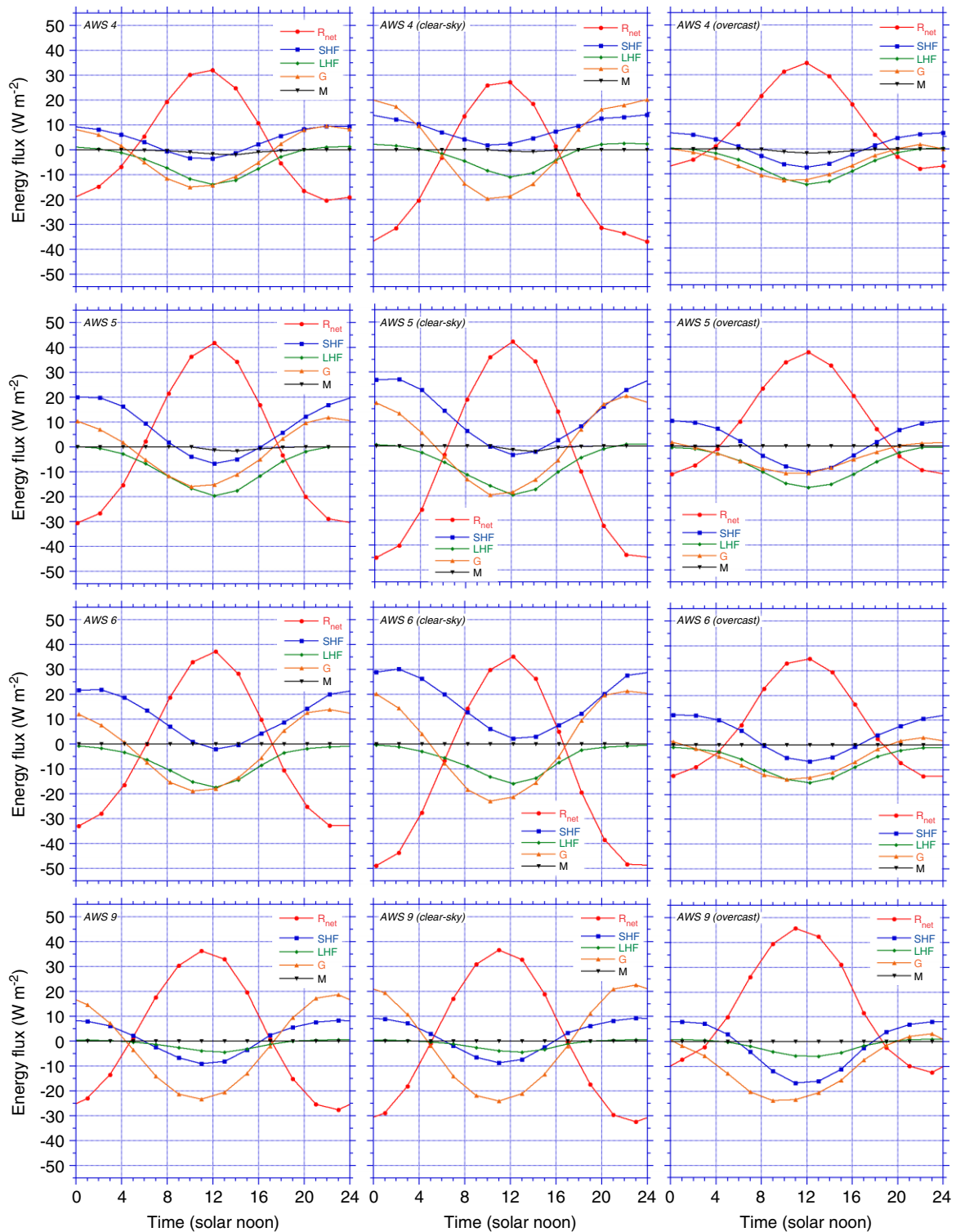
Figure 9. Average daily cycle of SEB components at AWS 4 (upper row), AWS 5 (second row), AWS 6 (third row) and AWS 9 (last row) for all-sky conditions (left column), clear-sky conditions (middle column) and overcast conditions (right column). This figure is available in colour online at www.interscience.wiley.com/ijoc

of SHF mainly depends on u_*; the largest values are found in the katabatic wind zone at AWS 5 and 6 ($> = 20$ W m^{-2}) and the smallest values at AWS 9 (<10 W m^{-2}).

Under clear-sky conditions the effect of increased θ_* generally exceeds that of decreased u_*, so that night-time SHF increases and achieves values of 30 W m^{-2} at AWS 6. Conversely, cloudy conditions decrease θ_* throughout the day, decreasing night-time stability and increasing the length and intensity of the convective period (negative SHF) around noon. It is remarkable that the strongest convection is found during overcast conditions on the interior plateau (AWS 9), with values of SHF < -15 W m^{-2}. During the night, clouds substantially decrease radiative cooling and therewith θ_*. Only at AWS 9 is the increase in u_* sufficient to compensate for this; at the other sites, night-time SHF decreases markedly under overcast conditions.

3.5. Latent heat flux (LHF)

Conditions in Antarctica are unfavourable for snow sublimation, in spite of the fact that the surface is always at saturation. Low temperatures limit air moisture content so that the vertical moisture gradient (q_*) is small (Figure 8). Moreover, in Antarctica the surface is often colder than the air, and air RH is high (75–91%, Table IV), reducing surface to air moisture gradients. Nonetheless, because all other SEB fluxes are also small, all-sky LHF is a major heat loss on a daily averaged basis (Table IV). This is also valid on sub-daily timescales for AWS 4, 5 and 6 with LHF reaching values of -15 to -20 W m^{-2} around noon (Figure 9). At AWS 9, the magnitude of noontime LHF remains below 5 W m^{-2} owing to low temperatures and wind speed at that site.

At AWS 4 and 9, q_* is rather insensitive to changes in the cloud cover (Figure 8). The increase in RH (which decreases q_*) is partly offset by the effect of higher temperatures (increasing q_*). Compared to clear-sky conditions, the increase in u_* under overcast conditions leads to an increase of LHF at AWS 4 and 9. At AWS 5 and 6, changes in u_* and q_* with cloudiness tend to counteract so that LHF remains relatively unchanged.

3.6. Sub-surface heat flux (G)

During summer, the daily average surface temperature exceeds snow temperatures so that all-sky daily average G is negative, acting to transport heat away from the surface into the snowpack (Table IV). For all-sky conditions, G has a pronounced daily cycle that takes on both significant positive and negative values, in contrast to SHF and LHF (Figure 9). Under clear-sky conditions, G attains an amplitude of about 20 W m^{-2}, which makes it the dominant daytime heat loss at all sites and the dominant night-time heat gain at AWS 4 and 9. Under overcast conditions, surface temperatures are anomalously high and daily mean G acts as a surface heat loss (Table IV), because the night-time values are close to zero. At daytime, G becomes less negative compared to all-sky conditions. At AWS 9, G remains the dominant (and from 3 a.m. to 6 a.m. even the only) surface heat sink, while at AWS 4, 5 and 6 it remains an important surface heat sink.

3.7. Melt (M)

Melting occurs when the surface temperature reaches 273.16 K, after which excess energy is invested in fusion. In the four-year period under consideration (1998–2001), 36 melt days occurred at AWS 4, 28 at AWS 5, 1 at AWS 6 and none at AWS 9. Although of some importance to the *mass balance* of the dry Antarctic climate (Van den Broeke *et al*., 2004a), melting is a small term in the average summertime SEB. Daily average $M < 1$ W m^{-2} at all sites is therefore not included in Table IV. On sub-daily timescales, the largest values are found at 14 h during clear-sky conditions at AWS 5, about 2 W m^{-2} (Figure 9). These non-zero values in the average daily cycle are manifestations of infrequent melt events associated with warm air advection and/or clear-sky conditions with little wind.

4. DISCUSSION AND CONCLUSIONS

We presented the daily cycle of the summertime (Julian days 296 to 51) Antarctic SEB and the influence of cloud cover. AWS data from four climatologically distinct regions were used: the coastal ice shelf (AWS 4, 34 m asl), the coastal katabatic wind zone (AWS 5, 363 m asl), the interior katabatic wind zone (station 6, 1160 m asl) and the interior plateau (AWS 9, 2892 m asl). To study the influence of cloud cover on the SEB, a division was made between all-sky, clear-sky and overcast conditions, based on a parameterisation using net long wave radiation (LW_{net}) as predictor.

Net short wave radiation (SW_{net}) is the major surface heat gain. Especially at elevated sites, clear-sky atmospheric transmissivity for short wave radiation, τ, is high (>80%), because clouds are few and optically thin and the atmosphere contains little water vapour and aerosol. Clouds influence SW_{net} in several ways: they enhance multiple scattering, increase snowfall frequency and increase surface albedo by altering the spectrum of SW radiation reaching the surface. Because average cloudiness, N, increases going from the interior (33% at AWS 9) towards the coast (54% at AWS 4), atmospheric transmissivity for short wave radiation, τ, decreases from 79% in the interior to 64% at the coast. Under clear-sky conditions, SW_{net} peaks in the katabatic wind zone in which snow metamorphosis is fast and albedo relatively low ($\alpha < 0.82$).

Net longwave radiation (LW_{net}) is the major surface heat loss. For all-sky conditions, daily averaged LW_{net} fully compensates the net gain by SW_{net}, so that the average net all-wave radiation (R_{net}) is essentially zero. However, R_{net} has a significant daily cycle with an amplitude of typically 30 W m^{-2} and drives the daily SEB cycle, with all other components tending to compensate. Noon time R_{net} is greatest at AWS 5 (41 W m^{-2}) and smallest at AWS 4 (31 W m^{-2}). At night, the largest radiative heat loss occurs at AWS 6 (−33 W m^{-2}) and the smallest at AWS 4 (−20 W m^{-2}). R_{net} peaks well before the solar noon, as a result of the asymmetric distribution of LW_{net} around the solar noon. When only clear skies are considered (Figure 9), noontime R_{net} values are similar to all-sky values, but night-time radiative heat losses are far greater, up to −50 W m^{-2} at AWS 6. As a result, daily mean R_{net} becomes significantly negative near the coast and in the katabatic wind zone. For overcast conditions, an increase in noontime R_{net} (compared to all-sky values) is observed at AWS 9; at the other sites the daytime changes are small. However, all stations experience a considerable reduction of night-time radiative cooling compared to all-sky conditions. Under overcast conditions, daily average R_{net} becomes significantly positive at all sites (Table IV) and the duration of the period with positive R_{net} increases (Figure 5). Because surface temperature quickly reacts to variations in absorbed solar radiation, LW_{net} and SW_{net} (and therefore R_{net}) are significantly negatively correlated (Figure 10). Note that R_{net} increases with cloudiness, which is referred to as *the radiation paradox*. It is a common feature in the Polar Regions and results from the high surface albedo, which reduces the influence of changes in SW_{net} on the radiation balance (Ambach, 1974).

Because of wind packing, Antarctic snow is relatively dense with high thermal conductivity, typically 0.2 to 0.3 K W^{-1} m^{-1}. That is why G is the most effective SEB component to compensate R_{net} on sub-daily timescales, especially under clear-sky conditions. In the katabatic wind zone (AWS 5 and 6), G balances about 40% of R_{net}, at AWS 4 about 50% and at AWS 9 even 70%. The reason is that turbulent exchange (convection through SHF, sublimation through LHF) fails to effectively remove heat from the surface. As a result, very large temperature gradients can develop in the near-surface snow pack: $G = 25$ W m^{-2} corresponds to a near-surface temperature gradient of 1 K per cm.

During the night, when R_{net} is negative, heat is mainly re-supplied to the surface by the turbulent flux of sensible heat (SHF) and the sub-surface heat flux (G). At daytime, when R_{net} is positive, sublimation (negative LHF) and heat conduction into the snow (negative G) remove excess radiative heat from the surface. On the interior plateau, owing to the low temperatures and the smooth surface, turbulent fluxes are small and the relative importance of G increases. A negative SHF, signifying convection, is observed at all sites, but its magnitude is small. Under clear-sky conditions, R_{net} becomes more negative during the night, which is mainly compensated by an increase in SHF at AWS 4, 5 and 6 and an increase in G at AWS 9. The lower night-time temperatures make daytime convection cease at the lower stations, which is compensated by an increase in G. Overcast conditions considerably reduce night-time radiative cooling at all sites. In response, night-time SHF and G decrease and the duration and intensity of daytime convection increase at all sites.
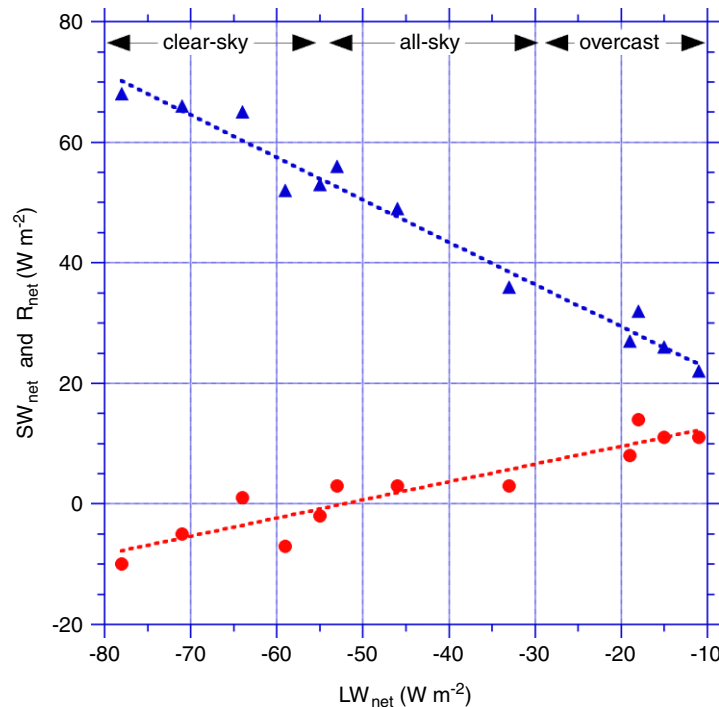
Figure 10. Correlation of net shortwave radiation (SW_{net}) and net all-wave radiation (R_{net}) with net longwave radiation (LW_{net}). Corresponding cloud over intervals are indicated at top of graph. Each data point represents a number from Table IV. This figure is available in colour online at www.interscience.wiley.com/ijoc

The double wind speed maximum at AWS 6 results from a combination of katabatic forcing at night and enhanced influence of large-scale forcing at daytime when static stability decreases under the influence of SW radiation absorption at the surface (Van den Broeke and Bintanja, 1995). Nocturnal katabatic flows play an important role in the daily SEB cycle; they are responsible for a night-time maximum in friction velocity, enhanced *SHF* as well as long wave radiative heat loss (Van den Broeke *et al*., 2004c). Unfortunately, from near-surface AWS measurements alone it is not possible to quantify the forcing mechanisms that determine the daily cycle of wind speed in the surface layer. Detailed profiling near AWS 9 up to 500 m above the surface with a tethered balloon has revealed a complex mix of katabatic forcing, inertial oscillations and stability-related curvature of the wind profile (Van As *et al*., 2006; Van As and van den Broeke, 2006). This shows that, in spite of the improved reliability and usefulness of Antarctic AWS for the calculation of the Antarctic near-surface climate and SEB, the need remains for detailed, on-site, boundary-layer experiments. Only then will we be able to fully understand the processes in the Antarctic surface layer.

REFERENCES

Allison I. 1985. Diurnal variability of the surface wind and air temperature at an inland Antarctic site: 2 years of AWS data. In *Australian Glaciological Research, 1982–1983*, ANARE Research Notes 28, edited by Jacka TH Australian Antarctic Division: Hobart, Australia, 81–92.

Ambach W. 1974. The influence of cloudiness on the net radiation balance of a snow surface with high albedo. *Journal of Glaciology* **13**: 73–84.

Anderson EA. 1976. A point energy and mass balance model of a snow cover. NOAA Technical report NWS19. National Oceanic and Atmospheric Administration: Silver Spring, USA.

Anderson PS. 1994. A method for rescaling humidity sensors at temperatures well below freezing. *Journal of Atmospheric and Oceanic Technology* **11**: 1,388–1,391.

Andreas EL. 1987. A theory for the scalar roughness and the scalar transfer coefficients over snow and sea ice. *Boundary-Layer Meteorology* **38**: 159–184.

Andreas EL. 2002. Parameterizing scalar transfer over snow and ice: a review. *Journal of Hydrometeorology* **3**: 417–432.

Argentini S, Viola A, Sempreviva AM, Petenko I. 2005. Summer boundary-layer height at the plateau site of Dome C, Antarctica. *Boundary-Layer Meteorology* **115**: 409–422.

Bintanja R. 2000. Surface heat budget of Antarctic snow and blue ice: interpretation of spatial and temporal variability. *Journal of Geophysical Research* **105**: 24 387–24 407.

Bintanja R, van den Broeke MR. 1995. The surface energy balance of Antarctic snow and blue ice. *Journal of Applied Meteorology* **34**: 902–926.

Brandt RE, Warren SG. 1993. Solar heating rates and temperature profiles in Antarctic snow and ice. *Journal of Glaciology* **39**: 99–110.

Clow GD, McKay CP, Simmons GM Jr, Wharton RA Jr. 1988. Climatological observations and predicted sublimation rates at Lake Hoare, Antarctica. *Journal of Climate* **1**: 715–728.

Dyer AJ. 1974. A review of flux-profile relationships. *Boundary-Layer Meteorology* **7**: 363–372.

Egger J. 1985. Slope winds and the axisymmetric circulation over Antarctica. *Journal of the Atmospheric Sciences* **42**: 1859–1867.

Gallée H, Schayes G. 1992. Dynamical aspects of katabatic winds evolution in the Antarctic coastal zone. *Boundary-Layer Meteorology* **59**: 141–161.

Hatzianastassiou N, Matsoukas C, Hatzidimitriou D, Pavlakis C, Drakakis M, Vardavas I. 2004. Ten year radiation budget of the Earth: 1984–1993. *International Journal of Climatology* **24**: 1785–1802.

Heinemann G. 1988. On the structure and energy budget of the boundary layer in the vicinity of the filchner ronne ice shelf front (Antarctica). *Beitrage zur Physik der Atmosphare* **61**(3): 244–258.

Heinemann G, Rose L. 1990. Surface energy balance, parametrizations of boundary-layer heights and the application of resistance laws near an Antarctic ice shelf front. *Boundary-Layer Meteorology* **51**: 123–158.

Holtslag AAM, De Bruijn EIF. 1988. Applied modelling of the nighttime surface energy balance over land. *Journal of Applied Meteorology* **27**: 689–704.

Kikuchi T, Ageta Y, Okuhira F, Shimamoto T. 1988. Climate and weather at the advanced camp in east Queen Maud Land, Antarctica. *Bulletin of Glacier Research* **6**: 17–25.

King JC, Anderson PS. 1994. Heat and water vapour fluxes and scalar roughness over an Antarctic ice shelf. *Boundary-Layer Meteorology* **69**: 101–121.

King JC, Connolley WM. 1997. Validation of the surface energy balance over the Antarctic ice sheets in the UK meteorological office unified climate model. *Journal of Climate* **10**: 1273–1287.

King JC, Connolley WM, Derbyshire SH. 2001. Sensitivity of modelled Antarctic climate to surface and boundary layer flux parametrizations. *Quarterly Journal of the Royal Meteorological Society* **127**: 779–794.

King JC, Argentini SA, Anderson PS. 2006. Contrasts between the summertime surface energy balance and boundary layer structure at Dome C and Halley stations, Antarctica. *Journal of Geophysical Research* **111**: D02105, DOI:10.1029/2005JD006130.

Liljequist GH. 1957. Energy exchange over an Antarctic snowfield: surface inversion and turbulent exchange. *Norwegian, British, Swedish Antarctic Expedition, 1949–1952. Scientific Results*, Vol. 2, Norsk Polarinstitutt: Oslo, Part 1d.

Mastrantonio G, Malvestuto V, Argentini S, Georgiadis T, Viola A. 1999. Evidence of a convective boundary layer developing on the Antarctic Plateau during the summer. *Meteorology and Atmospheric Physics* **71**: 127–132.

Ohata T, Kobayashi S, Ishikawa N, Kawaguchi S. 1985. Heat balance at the snow surface in a katabatic wind zone, East Antarctica. *Annals of Glaciology* **6**: 174–177.

Parish TR. 1992. On the role of Antarctic katabatic winds in forcing large-scale tropospheric motions. *Journal of the Atmospheric Sciences* **49**: 1374–1385.

Parish TR, Pettré P, Wendler G. 1993. A numerical study of the diurnal variation of the Adélie Land katabatic wind regime. *Journal of Geophysical Research* **98**(D7): 12933–12947.

Reijmer CH, Oerlemans J. 2002. Temporal and spatial variability of the surface energy balance in Dronning Maud Land, East Antarctica. *Journal of Geophysical Research* **107**: 4579–4770; DOI:10.1029/2000JD000110.

Renfrew IA, Anderson PS. 2002. The surface climatology of an ordinary katabatic wind regime in Coats Land, Antarctica. *Tellus* **54A**: 464–484.

Sorbjan Z, Kodama Y, Wendler G. 1986. Observational study of the atmospheric boundary layer over Antarctica. *Journal of Climate and Applied Meteorology* **25**: 641–651.

Stearns CR, Weidner GA. 1993. Sensible and latent heat flux estimates in Antarctica. In *Antarctic Meteorology and Climatology, Studies Based on Automatic Weather Stations*, *Antarctic Research Series*, Vol. 61. Bromwich DH, Stearns CR (eds). American Geophysical Union: Washington DC, USA; 109–138.

Van As D, van den Broeke MR. 2006. Structure and dynamics of the summertime atmospheric boundary layer on the Antarctic plateau, part II: Heat, momentum and moisture budgets. *Journal of Geophysical Research* in press.

Van As D, van den Broeke MR, van de Wal RSW. 2005a. Daily cycle of the surface energy balance on the high Antarctic plateau. *Antarctic Science* **17**(1): 121–133.

Van As D, van den Broeke MR, van de Wal RSW, Reijmer CH. 2005b. The summertime energy balance on the high Antarctic plateau. *Boundary-Layer Meteorology* **15**(2): 289–317, DOI: 10.1007/s10546-004-4631-1.
Van As D, van den Broeke MR, Helsen MM. 2006. Structure and dynamics of the summertime atmospheric boundary layer on the Antarctic plateau, part I: measurements and model validation. *Journal of Geophysical Research* in press.
Van den Broeke MR, Bintanja R. 1995. Summer time atmospheric circulation in the vicinity of a blue ice area in east Queen Maud Land, Antarctica. *Boundary-Layer Meteorology* **72**: 411–438.
Van den Broeke MR, van Lipzig NPM. 2002. Impact of vortex variability on the wintertime low-level climate of East Antarctica: results of a regional climate model. *Tellus* **54A**: 485–496.
Van den Broeke MR, Reijmer CH, van de Wal RSW. 2004a. A study of the Antarctic mass balance using automatic weather stations. *Journal of Glaciology* **50**(171): 565–582.
Van den Broeke MR, van As D, Reijmer CH, van de Wal RSW. 2004b. Assessing and improving the quality of unattended radiation observations in Antarctica. *Journal of Atmospheric and Oceanic Technology* **21**(9): 1417–1431.
Van den Broeke MR, van As D, Reijmer CH, van de Wal RSW. 2004c. The surface radiation balance in Antarctica as measured with automatic weather stations. *Journal of Geophysical Research* **109**: D09103, DOI:10.1029/2003JD004394.
Van den Broeke MR, van As D, Reijmer CH, van de Wal RSW. 2004d. The seasonal cycle of the Antarctic surface energy balance. *Annals of Glaciology* in press.
Van den Broeke MR, van As D, Reijmer CH, van de Wal RSW. 2005. Sensible heat exchange at the surface of the Antarctic ice sheet. *International Journal of Climatology* **25**: 1080–1101.
Van Lipzig NPM, van Meijgaard E, Oerlemans J. 1999. Evaluation of a regional atmospheric model using measurements of surface heat exchange processes from a site in Antarctica. *Monthly Weather Review* **127**: 1994–2011.
Wendler G, Ishikawa N, Kodama Y. 1988. The heat balance of the icy slope of Adélie Land, Eastern Antarctica. *Journal of Applied Meteorology* **27**: 52–65.
Zhang YC, Rossow WB, Lacis AA, Oinas V, Mishchenko MI. 2004. Calculation of radiative fluxes from the surface to top of atmosphere based on ISCCP and other global data sets: Refinements of the radiative transfer model and the input data. *Journal of Geophysical Research* **109**: D19105, DOI:10.1029/2003JD004457.